

Theoretical analysis of nonlinear fluid–structure interaction between large-scale polymer offshore floating photovoltaics and waves

Xu, P.; Wellens, P.R.

DOI

[10.1016/j.oceaneng.2022.110829](https://doi.org/10.1016/j.oceaneng.2022.110829)

Publication date

2022

Document Version

Final published version

Published in

Ocean Engineering

Citation (APA)

Xu, P., & Wellens, P. R. (2022). Theoretical analysis of nonlinear fluid–structure interaction between large-scale polymer offshore floating photovoltaics and waves. *Ocean Engineering*, 249, Article 110829. <https://doi.org/10.1016/j.oceaneng.2022.110829>

Important note

To cite this publication, please use the final published version (if applicable). Please check the document version above.

Copyright

Other than for strictly personal use, it is not permitted to download, forward or distribute the text or part of it, without the consent of the author(s) and/or copyright holder(s), unless the work is under an open content license such as Creative Commons.

Takedown policy

Please contact us and provide details if you believe this document breaches copyrights. We will remove access to the work immediately and investigate your claim.



Theoretical analysis of nonlinear fluid–structure interaction between large-scale polymer offshore floating photovoltaics and waves

Pengpeng Xu^{*}, Peter R. Wellens

Maritime and Transport Technology Department, TU Delft, Leeghwaterstraat 17, Delft, 2628 CA, The Netherlands

ARTICLE INFO

Keywords:

Nonlinear fluid–structure interaction
Euler Bernoulli–von Kármán beam
Large-scale polymer offshore floating photovoltaics
Perturbation method

ABSTRACT

The present research analyzes the nonlinear fluid–structure interaction (FSI) of free surface waves with large-scale polymer offshore floating photovoltaics (LPOFPV). The floating structure is modeled as a nonlinear Euler Bernoulli–von Kármán (EBVK) beam coupling with water beneath. The EBVK theory takes the in-plane force into consideration to account for the moderately large deflection slopes in LPOFPV. A multi-time-scale perturbation method leads to hierarchic partial differential equations by introducing the wave steepness squared as the perturbation. The analytical solution of the proposed nonlinear FSI model is obtained up to the second order. Pontoon structures and LPOFPV are studied and compared. The asymptotic solution provides the expressions of the propagating wave through the coupled system and its frequency–amplitude dispersion relation in a closed-form. A property of the solution is that the progressive plane wave through the coupled system remains linear for small dimensionless amplitudes, and features a second order correction for moderately large dimensionless amplitudes. Furthermore, it is also theoretically proven that no resonance occurs in the considered infinite problem. The proposed approach can be extended to the nonlinear coupling between a EBVK beam and Stokes waves.

1. Introduction

This article analytically investigates the hydro-elastic wave in an infinite model for large-scale polymer offshore floating photovoltaics (LPOFPV) that are an application of very large floating structures (VLFS).

The concept of VLFS has invoked the interest of academia over at least 50 years (Suzuki et al., 2006). In the past two decades, installations of large-scale floating solar farms (Trapani and Redón Santafé, 2015; Sahu et al., 2016; Ikhenicheu et al., 2021) have been proving their feasibility and applicability in industrial practice compared to other VLFS applications such as floating airports (Zhang et al., 2017; Yesudian and Dawson, 2021), floating bridges (Cheng et al., 2018), multi-purpose floating structures (Ren et al., 2019), etc. Those VLFS are still in the conceptual phase.

The dynamics of VLFS can be modeled as waves on an elastic sheet resting on the sea surface. We have identified two major approaches to construct the coupled governing equations. The first one is the curvature-dominant model (Forbes, 1986, 1988; Balmforth and Craster, 1999; Părău and Dias, 2002; Vanden-Broeck and Părău, 2011). The formulae were established based on the curvature expression because the considered structural material cannot endure relatively large transverse deformation. These models are mostly applied in ice engineering. Under

some conditions, inertia was neglected in these models (Părău and Dias, 2002; Vanden-Broeck and Părău, 2011).

The other category is applied for artificial floating structures that can endure more considerable bending. Since the turn of century, VLFS were generally modeled as one or multiple segments of flexible or even rigid beams and/or plates. The Euler Bernoulli (EB) beam became a popular option for the two-dimensional (2D) FSI problems. Many articles with floating support structures for offshore solar farms apply this linear beam model.

To study the influence of structural lengths on hydro-elastic properties of VLFS, Suzuki et al. (1996) proposed to model VLFS as a beam on an elastic foundation. Wang and Meylan (2002) considered the FSI problem of floating plates and gave a solution of linear FSI waves on a finite floating plate in an infinite water domain with variable depth. The result was numerically computed with a boundary element method (BEM). Later on, Chen et al. (2003) coupled the von Kármán plate with linear wave forces and numerically calculated the floating structure response to multi-directional waves. Cheng et al. (2014, 2016a,b) combined a linear structural model and a nonlinear wave model. They investigated the time-domain FSI dynamics of VLFS edged with perforated and non-perforated plates and their combination with analytical, numerical, and experimental methods. In their theoretical part, the

^{*} Corresponding author.

E-mail address: xupengpeng23418@icloud.com (P. Xu).



Fig. 1. Large-scale polymer offshore floating structure for photovoltaics. The large floating polymer membrane provides the foundation for photovoltaic panels. Source: Ocean Sun (2021).

finite length of the structure enabled the modal expansion technique essential for the FSI analysis. Cheng et al. (2017) applied EBVK into the numerical simulation utilizing a nonlinear numerical wave tank. The numerical tool was based on a higher-order BEM. The research objective was to investigate the nonlinear interaction between the structure and water waves traveling over a dam-shaped bathymetry. Their results showed that the influence of structural nonlinearity increased with waves propagating along the submerged breakwater. When traveling along the seaward slope, the primary wave dominated, and the higher harmonics significantly increased when arriving at the leeward slope. More recent research on the FSI model of pontoon-type structures can be found in Ilyas et al. (2018), Singla et al. (2018), Koley (2020), Liu et al. (2020), Karperaki and Belibassakis (2021), Meylan (2021), all of which applied the EB beam and potential flow.

Many studies investigate the hydro-elastics of continuous floating structures by locally coupling a finite structure and an infinite or semi-infinite water domain. Belibassakis and Athanassoulis (2005) proposed a method worthy of attention that expanded the local-mode series of the wave potential and coupled it with the finite linear beam. The system formed a local-global model for the infinite problem. A similar modal coupling principle was also applied to investigate dispersion relations of floating structures modeled by Rayleigh beam theory and thick beam theory (Athanassoulis and Belibassakis, 2009; Papathanasiou and Belibassakis, 2014).

In recent years, plate-array floating structures gained researchers' interest. The model can be seen as multiple beam segments with connections in between. Riyansyah et al. (2010) implemented a numerical scheme to study the optimal design of the connection between two floating beam segments. The beam was modeled by EB and discretized with the finite element method (FEM), while the water was modeled by potential theory and discretized with BEM. Iijima and Fujikubo (2018) numerically and experimentally investigated the hydro-elastoplasticity of a floating structure with two elastic segments connected with a plastic hinge. The linear potential with BEM represented the hydrodynamics, while the beam with FEM described the structural dynamics. Iijima and Fujikubo (2019) analytically investigated the same model in which the hydrodynamic force was modeled as a distributed spring.

The literature shows that (a) fully analytical models for wave-beam interaction problems in infinite domains are rare and (b) many studies were based on the numerical computation by means of BEM.

Large-scale polymer offshore floating photovoltaics (LPOFPV) were successfully deployed in industrial projects, as illustrated in Fig. 1. The smaller stiffness of the polymer membrane results in moderately large

bending deflections and strong hydro-elastic interaction with water waves (Schreier and Jacobi, 2020). As indicated by Magkouris et al. (2021), the response of floating solar to waves has a non-negligible influence (0 to 15%) on the performance of photovoltaic production. Hence, a better understanding and prediction of the hydro-elastic behavior of LPOFPV is needed. Compared with linear EB beam theory, EBVK introduces the nonlinearity in the in-plane strain-displacement relation, thus taking the effects of a moderately large slope and a membrane force into account. Hence, EBVK models LPOFPV better. At the same time, a small structural stiffness already is a filter for the depth of troughs and the acuteness of peaks associated with steeper free surface waves and modeled by nonlinear potential theory. It is reasonable to assume that the nonlinearity in water waves some distance away from the edge is small and thus negligible. Hence, linear potential (Airy) theory is applicable in the large part of the structure away from the edges. Therefore, we propose to combine the EBVK beam and Airy waves to formulate the infinite FSI problem for LPOFPV. Our nonlinear structure-linear water model can be considered complementary to the linear structure-nonlinear water model proposed by Ma et al. (2020) for pontoon-type VLFS.

In a this recent study, Ma et al. (2020) derived a fully analytical solution up to the second order by coupling a linear EB beam with nonlinear potential waves. Numerical simulation was also performed with a weakly coupled algorithm using FEM for the beam and smoothed-particle hydrodynamics (SPH) for water. Significant findings were (a) that there existed a critical wave period and (b) that steeper crests and flatter troughs occurred when the incoming wave period was larger than the critical and vice versa.

In this article, we will seek a fully analytical solution of the combined theory of EBVK with Airy waves for the application of LPOFPV. Our objectives are: (a) to demonstrate the applicability of the proposed model for LPOFPV, (b) to study the influence of nonlinearity on the FSI waves, and (c) to investigate if resonance occurs in the considered problem in an infinite domain.

2. Theoretical model

Structurally, LPOFPV mainly consist of a membrane and a floating ring at the edge, see Fig. 1. The ring provides a protective environment for PV modules and keeps the membrane stretched. LPOFPV are usually deployed in coastal waters where long waves hardly occur. The structural length with a magnitude of over 50 meters at the present stage is large compared with the wavelengths. Therefore, it is assumed that edge-effects modeled by boundary conditions at the upstream side and the downstream side can be neglected. Other important assumptions are (a) that the structure is impenetrable and (b) that a vacuum does not occur. Thus, the LPOFPV can be modeled as a 2D EBVK beam in an infinite domain that considers geometrical nonlinearity because of the moderately large transverse deflections. Fig. 2 depicts the idealized 2D model of LPOFPV floating on the sea surface in an open area. Linear potential theory describes water motion. A train of waves traveling in horizontal direction through the coupled system is considered.

2.1. Governing equations

2.1.1. Nonlinear Euler Bernoulli-von Kármán theory for beam

The membrane material used in a LPOFPV, on which PV panels are installed, has less bending stiffness than steel used often for plates or beams. It experiences relatively large deflection in waves compared to metal structures (Schreier and Jacobi, 2020). The moderately large rotations and strains are non-negligible (Vadlamani and Arun, 2019). The nonlinearity in the EBVK beam model is derived by keeping the axial normal strain and neglecting other nonlinear terms (Paavani et al., 2020), which is representative of a membrane force. Neglecting the rotary inertia (Chia, 1980; Jang, 2013; Jain et al., 2018; Krysko et al.,

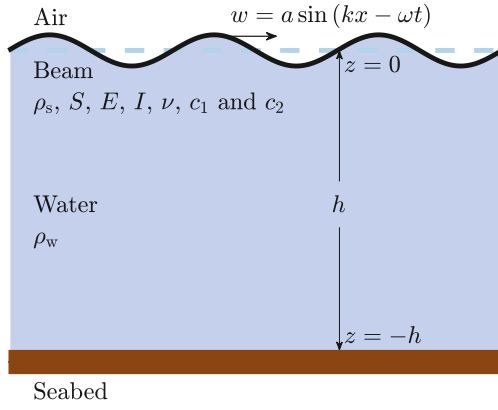


Fig. 2. The 2D sketch of LPOFPV floating on the sea surface. The structure is modeled by an EBVK beam, moving together with water waves.

2018; Xu and Wellens, 2021), the equation of motion (EOM) of the EBVK beam reads

$$\rho_s S \frac{\partial^2 w}{\partial t^2} + EI \frac{\partial^4 w}{\partial x^4} - \frac{3}{2} SE \left(\frac{\partial w}{\partial x} \right)^2 \frac{\partial^2 w}{\partial x^2} + c_1 b \frac{\partial w}{\partial t} + c_2 b \frac{\partial^5 w}{\partial t \partial x^4} = q_w. \quad (1)$$

The beam has material density ρ_s , cross-section area $S = bd$, Young's modulus E and inertial moment $I = \frac{bd^3}{12(1-\nu^2)}$. Here, d stands for the beam thickness (in z -direction), b for the beam width and ν for the Poisson ratio. c_1 and c_2 are the external and internal damping coefficients (Banks et al., 1994) with units $[\text{N s/m}^2]$ and $[\text{N m s}]$, considered per unit area. w is the transverse displacement of the beam. The external distributed load q is the hydrodynamic load when assuming initial floating equilibrium. Note that q has unit $[\text{N/m}]$ because the load is distributed over length in the 1D beam model.

2.1.2. Linear potential theory for water

The water has density ρ_w and uniform depth h . Linear potential theory gives the governing equations of the inviscid, irrotational and incompressible flow

$$\frac{\partial^2 \phi}{\partial x^2} + \frac{\partial^2 \phi}{\partial z^2} = 0, \quad (2)$$

where ϕ represents the fluid velocity potential.

The seabed is impenetrable at the bottom:

$$\frac{\partial \phi}{\partial z} = 0 \quad \text{at} \quad z = -h, \quad (3)$$

where h is the uniform water depth.

At the free surface, the kinematic boundary condition reads

$$\frac{\partial \eta}{\partial t} = \frac{\partial \phi}{\partial z} \quad \text{at} \quad z = 0, \quad (4)$$

where η stands for the free surface elevation. And the Bernoulli equation gives the dynamic boundary condition:

$$p + \rho_w \frac{\partial \phi}{\partial t} + \rho_w g \eta = 0 \quad \text{at} \quad z = 0, \quad (5)$$

where p is the water pressure with unit $[\text{N/m}^2]$, and $g = 9.81 \text{ m/s}^2$ is the acceleration of gravity.

2.1.3. FSI equations

The beam and water models are coupled through the interface conditions:

$$w = \eta \quad \text{and} \quad q_w = pb \quad \text{at} \quad z = 0. \quad (6)$$

Note that the distributed force on the beam is obtained from multiplying the hydrodynamic pressure p with the beam width b for consistency of the unit $[\text{N/m}]$.

Fluid and structure are coupled at the free surface, leading to:

$$\frac{\partial w}{\partial t} = \frac{\partial \phi}{\partial z} \quad \text{at} \quad z = 0 \quad (7)$$

and

$$\rho_s d \frac{\partial^2 w}{\partial t^2} + \frac{Ed^3}{12(1-\nu^2)} \frac{\partial^4 w}{\partial x^4} - \frac{3}{2} Ed \left(\frac{\partial w}{\partial x} \right)^2 \frac{\partial^2 w}{\partial x^2} + \rho_w g w + \rho_w \frac{\partial \phi}{\partial t} + c_1 \frac{\partial w}{\partial t} + c_2 \frac{\partial^5 w}{\partial t \partial x^4} = 0. \quad (8)$$

Here, S , I and η have been replaced or eliminated by $S = bd$, $I = \frac{bd^3}{12(1-\nu^2)}$ and Eq. (6).

2.2. Normalization

Introducing the normalized variables

$$\begin{cases} X = kx, & Z = kz, & \tau = kt, & \varepsilon = A^2 k^2, & H = kh, \\ \kappa = \frac{d^2 k^2 E}{12(1-\nu^2) \rho_s}, & \alpha = \frac{3E}{2\rho_s}, & \beta = \frac{\rho_w g}{\rho_s d k^2}, & \sigma = \frac{c_1}{\varepsilon \rho_s d k}, & \zeta = \frac{k^3 c_2}{\varepsilon \rho_s d}, \\ W(X, \tau) = \frac{w(X, \tau)}{A} & \text{and} & \Phi(X, Z, \tau) = \frac{k}{Ag} \phi(X, Z, \tau), \end{cases} \quad (9)$$

in which A and k are the wave amplitude and wave number. The perturbation $\varepsilon = A^2 k^2$ equivalently represents the wave steepness squared. Note that here we introduce the new damping coefficients σ and ζ to scale two kinds of damping to the same degree of nonlinearity. This treatment is credible because (a) the external and internal damping coefficients are small, usually in the order of a percent or even lower than one percent, (b) the effect of damping (energy dissipation) on wave propagation is part of the scope of this study, and not the exact numbers for the type of material in LPOFPV.

Substitution of Eq. (9) into Eqs. (7) and (8) yields the normalized EOM for the nonlinear FSI system:

$$\frac{\partial^2 \Phi}{\partial X^2} + \frac{\partial^2 \Phi}{\partial Z^2} = 0 \quad (10)$$

$$\frac{\partial \Phi}{\partial Z} \Big|_{Z=-H} = 0 \quad (11)$$

$$\frac{\partial W}{\partial \tau} - \frac{g}{k} \frac{\partial \Phi}{\partial Z} \Big|_{Z=0} = 0 \quad (12)$$

$$\frac{\partial^2 W}{\partial \tau^2} + \kappa \frac{\partial^4 W}{\partial X^4} - \varepsilon \alpha \left(\frac{\partial W}{\partial X} \right)^2 \frac{\partial^2 W}{\partial X^2} + \beta W + \beta \frac{\partial \Phi}{\partial \tau} \Big|_{Z=0} \quad (13)$$

$$+ \varepsilon \sigma \frac{\partial W}{\partial \tau} + \varepsilon \zeta \frac{\partial^5 W}{\partial \tau \partial X^4} = 0$$

Eq. (13) demonstrates that the nonlinear term is of high order $\mathcal{O}(\varepsilon)$. In other words, the wave steepness squared $(ak)^2$ scales the nonlinearity. The nonlinear effect becomes significant for moderately large hydro-elastic waves, which is in agreement with the underlying assumptions of von Kármán theory.

3. Analytical solution

3.1. Multi-time-scale expansion

Introducing the multi-time-scale with the two-term expansion:

$$\tau \sim \tau_0 + \tau_1, \quad \tau_0 = \tau \quad \text{and} \quad \tau_1 = \varepsilon \tau. \quad (14)$$

Eq. (14) also expands partial differential operators acting on time τ :

$$\frac{\partial}{\partial \tau} \sim \frac{\partial}{\partial \tau_0} + \varepsilon \frac{\partial}{\partial \tau_1} + \mathcal{O}(\varepsilon^2) \quad \text{and} \quad \frac{\partial^2}{\partial \tau^2} \sim \frac{\partial^2}{\partial \tau_0^2} + 2\varepsilon \frac{\partial^2}{\partial \tau_0 \partial \tau_1} + \mathcal{O}(\varepsilon^2). \quad (15)$$

The as of yet undetermined solution of plane wave $W(X, \tau)$ is expanded accordingly:

$$W(X, \tau) \sim W_0(X, \tau_0, \tau_1) + \varepsilon W_1(X, \tau_0, \tau_1) + \mathcal{O}(\varepsilon^2). \quad (16)$$

Note that the water wave potential is linear and thus needs no solution expansion but only the time-scale expansion:

$$\Phi(X, Z, \tau) \sim \Phi(X, Z, \tau_0, \tau_1). \quad (17)$$

3.2. Hierarchical partial differential equations

Substituting Eqs. (14) and (16) into Eqs. (12) and (13) and collecting terms ϵ of the same order, yields a series of hierarchically linear partial differential equations (PDE) with nonlinear inhomogeneous terms on the right-hand side from the second-order on. Retaining up to the first order of perturbation:

$$\bullet \mathcal{O}(\epsilon^0)$$

$$\frac{\partial^2 \Phi}{\partial X^2} + \frac{\partial^2 \Phi}{\partial Z^2} = 0 \quad (18)$$

$$\left. \frac{\partial \Phi}{\partial Z} \right|_{Z=-H} = 0 \quad (19)$$

$$\left. \frac{\partial W_0}{\partial \tau_0} - \frac{g}{k} \frac{\partial \Phi}{\partial Z} \right|_{Z=0} = 0 \quad (20)$$

$$\frac{\partial^2 W_0}{\partial \tau_0^2} + \kappa \frac{\partial^4 W_0}{\partial X^4} + \beta W_0 + \beta \left. \frac{\partial \Phi}{\partial \tau_0} \right|_{Z=0} = 0 \quad (21)$$

$$\bullet \mathcal{O}(\epsilon^1)$$

$$\frac{\partial^2 W_1}{\partial \tau_0^2} + \kappa \frac{\partial^4 W_1}{\partial X^4} + \beta W_1 = \alpha \left(\frac{\partial W_0}{\partial X} \right)^2 \frac{\partial^2 W_0}{\partial X^2} - \beta \left. \frac{\partial \Phi}{\partial \tau_1} \right|_{Z=0} - \sigma \frac{\partial W_0}{\partial \tau_0} - \varsigma \frac{\partial^5 W_0}{\partial \tau_0 \partial^4 X} - 2 \frac{\partial^2 W_0}{\partial \tau_0 \partial \tau_1} \quad (22)$$

3.3. The first-order

3.3.1. The first-order solution in normalized form

First separate the potential into three parts, namely the time-dependent part $\varphi(\tau_0, \tau_1)$, the horizontal space-dependent part $\xi(X)$ and the vertical space-dependent part $\zeta(Z)$

$$\Phi(X, Z, \tau_0, \tau_1) = \varphi(\tau_0, \tau_1) \xi(X) \zeta(Z). \quad (23)$$

Substitution of Eq. (23) into Eqs. (18) and (19) yields

$$\Phi(X, Z, \tau_0, \tau_1) = \varphi(\tau_0, \tau_1) \cos(X) \cosh(Z + H). \quad (24)$$

Here, two arbitrary integral constants of $\xi(X)$ and $\zeta(Z)$ merge into the undetermined time-dependent function $\varphi(\tau_0, \tau_1)$. We also get rid of the arbitrary phase shift of $\xi(X)$ because only the plane propagating wave is of our interest.

Taking the partial derivative about τ_0 of Eq. (21) and using Eqs. (20) and (24), we obtain a linear ordinary differential equation (ODE) about $\varphi(\tau_0)$:

$$g \tanh(H) \frac{\partial^2 \varphi}{\partial \tau_0^2} + k\beta \frac{\partial^2 \varphi}{\partial \tau_0^2} + g\beta \tanh(H) \varphi + \kappa g \tanh(H) \varphi = 0. \quad (25)$$

The solution of Eq. (25) is

$$\varphi(\tau_0, \tau_1) = C_0(\tau_1) \cos \left(\sqrt{\frac{g \tanh(H) (\beta + \kappa)}{g \tanh(H) + k\beta}} \tau_0 + \Theta(\tau_1) \right), \quad (26)$$

in which $C_0(\tau_1)$ and $\Theta(\tau_1)$ are two arbitrary functions of the slow time scale τ_1 stemming from integration. The coefficient in front of the regular time scale τ_0 in Eq. (26) is the primary angular frequency

$$\Omega_0 = \sqrt{\frac{g \tanh(H) (\beta + \kappa)}{g \tanh(H) + k\beta}}. \quad (27)$$

Note that Eq. (27) is the linear dispersion relation in normalized form.

Combining Eqs. (24) and (26) into a right-ward propagating wave as shown in Fig. 2, gives

$$W_0(X, \tau_0, \tau_1) = A_0(\tau_1) \cos(X - \Omega_0 \tau_0 + \Theta(\tau_1)) \quad (28)$$

and

$$\Phi(X, Z, \tau_0, \tau_1) = A_0(\tau_1) \frac{k\Omega_0 \cosh(Z + H)}{g \sinh(H)} \sin(X - \Omega_0 \tau_0 + \Theta(\tau_1)), \quad (29)$$

in which

$$A_0(\tau_1) = \frac{g \sinh(H)}{k\Omega_0} C_0(\tau_1). \quad (30)$$

Although Eqs. (28) and (29) gives the forms of the first order waves and potential, their amplitude $A_0(\tau_1)$ and phase shift $\Theta(\tau_1)$ are unknown functions of the slow time scale τ_1 . The unknown functions will be solved to second order, see Section 3.4.

3.3.2. The first-order solution in original form

The linear dispersion relation is widely used in engineering. Hence we would like to explicitly give the linear expression in dimensional form by inversely utilizing Eq. (9):

$$\omega_0 = k \sqrt{\frac{g \tanh(kh) \left(\frac{\rho_w g}{\rho_s k^2 d} + \frac{k^2 d^2 E}{12 \rho_s (1 - \nu^2)} \right)}{\frac{\rho_w g}{\rho_s k d} + g \tanh(kh)}}. \quad (31)$$

3.4. The second-order

3.4.1. The second-order solution in normalized form

The first-order solution Eqs. (28) and (29) is substituted into the right-hand-side of Eq. (22) and then terms with the same trigonometric functions are collected. There exist primary trigonometric terms, i.e., $\sin(X - \Omega_0 \tau_0 + \Theta(\tau_1))$ and $\cos(X - \Omega_0 \tau_0 + \Theta(\tau_1))$. Their coefficients are respectively

$$C_{\sin} = \frac{\beta k \Omega_0}{g \tanh(H)} \frac{\partial A_0}{\partial \tau_1} + (\sigma + \varsigma) \Omega_0 A_0 + 2\Omega_0 \frac{\partial A_0}{\partial \tau_1} \quad (32)$$

and

$$C_{\cos} = -\frac{\alpha}{4} A_0^3 - \frac{\beta k \Omega_0}{g \tanh(H)} \frac{\partial \Theta}{\partial \tau_1} - 2\Omega_0 A_0 \frac{\partial \Theta}{\partial \tau_1}. \quad (33)$$

Avoiding secular terms requires

$$C_{\sin} = 0 \quad \text{and} \quad C_{\cos} = 0. \quad (34)$$

Eqs. (32) and (34) can solve $A_0(\tau_1)$:

$$A_0(\tau_1) = A \exp \left\{ -\frac{g \tanh(H)}{\beta k + 2g \tanh(H)} (\sigma + \varsigma) \tau_1 \right\}, \quad (35)$$

where A is the constant wave amplitude independent of the slow time-scale τ_1 .

Substitution of Eq. (35) into Eq. (33) leads to

$$\Theta(\tau_1) = \frac{A^2 \alpha}{8\Omega_0 (\sigma + \varsigma)} \exp \left\{ -\frac{2g \tanh(H)}{\beta k + 2g \tanh(H)} (\sigma + \varsigma) \tau_1 \right\} + C_1. \quad (36)$$

Next, we simplify the exponential part of Eq. (36) by a Taylor expansion around the small damping $\sigma + \varsigma \approx 0$, and then get rid of the constant part by setting the arbitrary integral constant C_1 to zero. After these manipulations, we obtain

$$\Theta(\tau_1) = -\frac{A^2 \alpha g \tanh(H)}{4\Omega_0 (\beta k + 2g \tanh(H))} \tau_1. \quad (37)$$

Eq. (37) is substituted back into the first-order solution Eq. (28). The solution of the propagating wave then reads

$$W_0 = A_0(\tau_1) \cos \left(X - \Omega_0 \tau - \frac{A^2 \alpha g \tanh(H)}{4\Omega_0 (\beta k + 2g \tanh(H))} \epsilon \tau \right). \quad (38)$$

$$w_1(x, t) = \varepsilon A \frac{3Edk^2(1-\nu^2)(\tanh(kh)dk\rho_s + \rho_w)}{54Ed^3k^4\rho_w + 8(1-\nu^2) + 48\rho_s kd \tanh(kh)\left(d^3k^4E - \frac{4}{3}g\rho_w(1-\nu^2)\right)} \exp\left\{-3\varepsilon \frac{\rho_s g k(\sigma + \zeta)}{\frac{\rho_w g}{dk} + 2\rho_s g \tanh(kh)} t\right\} \cos(3kx - 3\omega t) \quad (43)$$

Box I.

Therefore, the nonlinear angular frequency up to the second-order is

$$\Omega = \Omega_0 + \frac{\varepsilon A^2 \alpha g \tanh(H)}{4\Omega_0(\beta k + 2g \tanh(H))}. \quad (39)$$

Substituting Eqs. (35), (37) and (39) into the second-order surface dynamic condition Eq. (22), we obtain, after some manipulation, the second-order wave:

$$W_1(X, \tau_0, \tau_1) = A_1(\tau_1) \cos(3X - 3\Omega\tau_0), \quad (40)$$

whose amplitude equals

$$A_1(\tau_1) = \frac{A_0^3(\tau_1) \alpha}{4(-9\Omega_0 + \beta + 81\kappa)}. \quad (41)$$

3.4.2. The second-order solution in original form

For the convenience of engineering practice, we give the expression of the second-order nonlinear solutions in dimensional form. The normalized arbitrary amplitude A is set to 1 for generality. In addition, we choose to keep the damping terms in the normalized form, i.e., σ and ζ for simplicity because damping values are out of interest of the present work.

- The first-order wave

$$w_0(x, t) = A \exp\left\{-\varepsilon \frac{\rho_s g k(\sigma + \zeta)}{\frac{\rho_w g}{dk} + 2\rho_s g \tanh(kh)} t\right\} \cos(kx - \omega t) \quad (42)$$

- The second-order wave (see Eq. (43) in Box I).
- The nonlinear dispersion relation

$$\omega = k \sqrt{\frac{g \tanh(kh) \left(\frac{\rho_w g}{\rho_s k^2 d} + \frac{k^2 d^2 E}{12\rho_s(1-\nu^2)} \right)}{\frac{\rho_w g}{\rho_s kd} + g \tanh(kh)}} + \varepsilon k \frac{3E \sqrt{g \tanh(kh) \left(\frac{\rho_w g}{\rho_s kd} + g \tanh(kh) \right)}}{8\rho_s \left(\frac{\rho_w g}{\rho_s kd} + 2g \tanh(kh) \right) \sqrt{\frac{\rho_w g}{\rho_s k^2 d} + \frac{k^2 d^2 E}{12\rho_s(1-\nu^2)}}} \quad (44)$$

One can readily construct the expression of the two-term asymptotic solution according to Eqs. (9) and (16).

4. Case study and discussion

We perform a case study on two typical conditions by choosing the values of the physical parameters according to two recently published papers. The upper part of Table 1 gives parameters for metal pontoon structures used by Ma et al. (2020). We will name this Case A. The pontoon-type VLFS is a multi-hollow structure, typically consisting of buoyancy boxes and stiffness girders. We simplify the deformation of the VLFS as the transverse deflection of a beam in our 2D model, which is consistent with the simplification of Ma et al. (2020). Note that these physical parameters are adapted from and equivalent to but not exactly equal because of different notations and units. The lower part of Table 1 contains parameters for LPOFPV tested by Schreier and Jacobi (2020), named Case B from here on. The latter article describes model tests to investigate the hydro-elastic interaction of a polymer film with water waves.

Table 1
Physical parameters of Case A and Case B.

Case description	Symbol	Value	Unit
Case A Metal pontoon for VLFS (Ma et al., 2020)	ρ_s	6.0×10^2	kg/m ³
	d	2.0×10^{-2}	m
	E	1.6416×10^6	Pa
	ν	3.0×10^{-1}	–
	ρ_w	1.025×10^3	kg/m ³
	h	8.0×10^{-1}	m
Case B Polymer film for LPOFPV (Schreier and Jacobi, 2020)	ρ_s	1.16×10^2	kg/m ³
	d	5.0×10^{-3}	m
	E	5.6×10^5	Pa
	ν	4.0×10^{-1}	–
	ρ_w	1.025×10^3	kg/m ³
	h	1.0×10^0	m

4.1. Smallness

The classical perturbation method establishes hierarchical PDEs in Section 2 and generates solutions in Section 3. This method mathematically requires the perturbation $\varepsilon \ll 1$. Considering that $\varepsilon = a^2 k^2$ (see Eq. (9)), the perturbation requires the square of the traveling wave slope ($a^2 k^2$) much smaller than one. Eliminating the square leads to the conclusion that the requirement on the wave slope is less strict. The perturbation method mathematically requires that the wave slope $\varepsilon = ak \ll 1$ in a model with a linear beam and a nonlinear water wave (see Schwartz, 1974; Dingemans, 1997). It is our argument that the model that couples the nonlinear beam with linear water has a larger range of application in terms of wave slopes than models with linearized beams.

4.2. Damping

Eqs. (37) and (44) imply that the damping does not affect the dispersion relation, or the phase velocity equivalently, up to second-order. Eqs. (42) and (43) show that wave amplitudes exponentially attenuate in the propagation direction due to damping that is represented by σ and ζ .

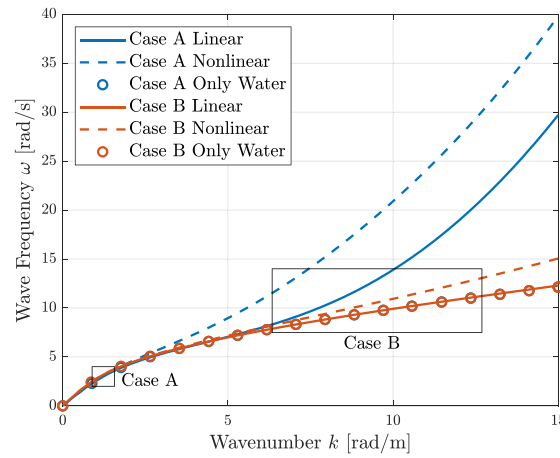
In absence of damping ($\sigma + \zeta = 0$), the nonlinear amplitude Eq. (35) becomes

$$A_0(\tau_1) = A, \quad (45)$$

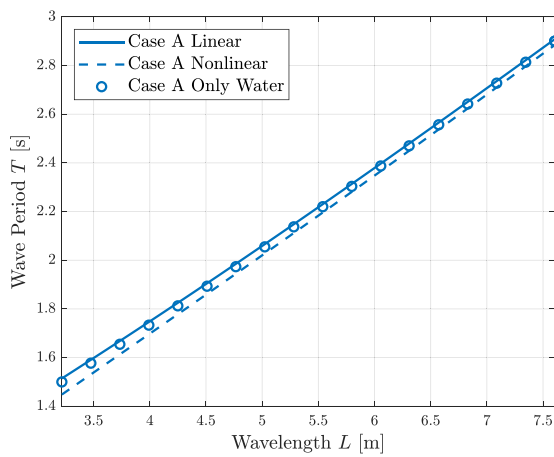
where A on the right-hand side is an arbitrary constant (see also Section 3.4.1). Eq. (45) indicates that the amplitude remains constant without damping. Note that the phase-shift solution Eq. (37) that is expanded with the Taylor series is equivalent to the solution of substituting Eq. (45) into Eqs. (32) and (33).

4.3. Dispersion relation

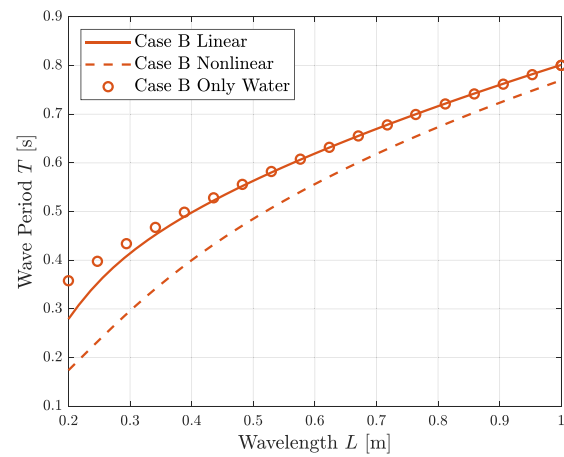
The dispersion relation is important in the problem of wave propagation. Eqs. (31) and (44) give the linear and nonlinear expressions of the hydro-elastic dispersion relation. In Eq. (44), the first term is the linear dispersion relation that is also given by Eq. (31) and the second term is the nonlinear correction. Fig. 3 illustrates both linear and nonlinear dispersion relations in Case A and Case B calculated by Eqs. (31) and (44).



(a) Comparison of Case A and Case B



(b) Case A



(c) Case B

Fig. 3. Dispersion relations of Case A (VLFS) and Case B (LPOFPV). (a) shows the overall reasonable range of wave numbers; (b) and (c) are the enlargements of Case A and Case B in (a), in which the wave length ranges are identical to those in Ma et al. (2020) and Schreier and Jacobi (2020) respectively. Note that the dispersion relation of wave period over wave length is equivalent to wave frequency over wave number.

4.3.1. Linear dispersion relation

Eq. (31) confirms that all physical parameters associated with FSI waves are positively defined. The positive definition proves that the floating structure always stiffens the hydro-elastic system, increasing the wave frequency.

Fig. 3 visualizes the linear dispersion relation calculated by Eq. (31) for Case A and Case B. Table 1, and Fig. 3(a) demonstrates that the stiffening effect in the hydro-elastic description of pontoon-type floating structures is significant, especially for shorter waves. In contrast, the change in wave propagation due to the film-type floating structure is relatively small. These phenomena are expected physically. The explanation is that the floating structure resists bending of the free surface, adding stiffness to the hydro-elastic system. The plate-like structure in Case A has a larger Young's modulus than the membrane-like structure in Case B. As a consequence, the pontoon makes the coupled system harder to bend, while the film almost follows the water waves. Figs. 3(b) and 3(c) indicate that the floating structures do not significantly affect the dispersion relation in the ranges chosen for Case A and Case B. Shorter waves could illustrate the effect of stiffening better: the hydro-elastic effect would be more pronounced from $k > 7$ rad/m on.

The dispersion relation in the case of only water is

$$\omega_{OW} = \sqrt{kg \tanh(kh)}, \quad (46)$$

Setting $\rho_s = E = 0$ in Eqs. (31) and (44) also leads to this expression. The two curves for Case A and Case B in the situation of only water without structure are almost equal to each other because of the water depths in the two cases being similar ($h_A = 0.8$ m and $h_B = 1$ m).

4.3.2. Nonlinear dispersion relation

Solutions in Section 3.4.1 show that all the nonlinear effects, including the nonlinear dispersion relation Eq. (44), are scaled by the perturbation ϵ , i.e., the wave steepness squared $(ak)^2$. Furthermore, Eq. (44) is also positively defined, which implies that an infinite phase velocity cannot occur in the nonlinear description of hydro-elastic waves either.

The nonlinear dispersion relations are illustrated in Fig. 3, in which Fig. 3(a) shows the range of wave lengths, Figs. 3(b) and 3(c) presents the same ranges in Case A and Case B, respectively. Because the wave steepness squared $\epsilon = (ak)^2$ scales the nonlinear solution, we plot Fig. 3 by fixing the perturbation $\epsilon = 0.01$ and varying the wave number k in ranges corresponding to literature. In other words, the amplitude decreases when the wave becomes shorter, keeping the same small steepness $ak = 0.1$. Take Case A for example, $k \in [0.8263, 1.9530]$ and $L \in [3.2172, 7.6036]$ corresponds to $T \in [1.5, 2.9]$ of Fig. 6 of Ma et al. (2020). Fig. 3 includes this range. Varying with k , wave amplitude $a \in [0.121, 0.0512]$ in Case A. The same applies to Case B.

Fig. 4 shows the nonlinear dispersion relations of Case A and Case B. The wave frequency ω varies with both the wave number k and

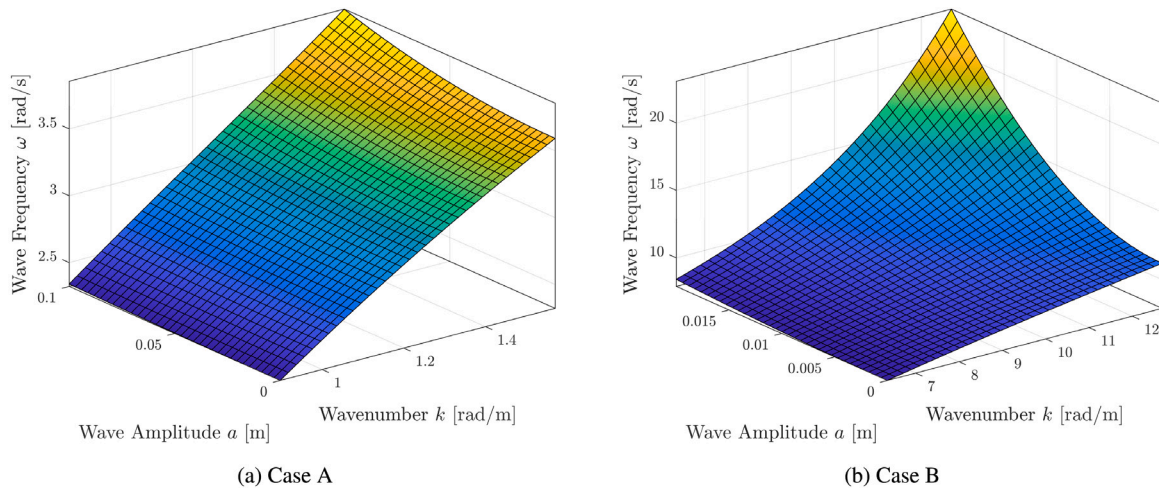


Fig. 4. Nonlinear dispersion relation given by Eq. (44) for Case A (VLFS) and case B (LPOFPV). The wavenumber and the first-order amplitude vary within the same range in both Case A and Case B, respectively.

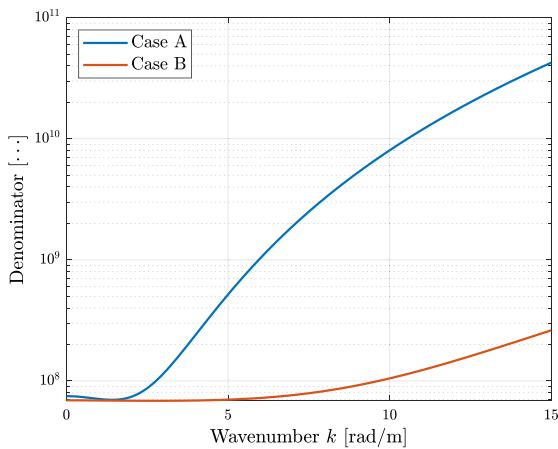


Fig. 5. The denominator in Eq. (43) over a large range of wave numbers. The unit of the ordinate is omitted because it is physically meaningless.

the first-order amplitude a . The range of k and the maximum of a are extracted from Case A and Case B, respectively; the minimum of a is set to zero to illustrate the linear dispersion relation. The nonlinear wave frequency monotonically increases with both the wave number and the first-order amplitude as indicated by the positively defined dispersion relation Eq. (44). Note that the perturbation contains the amplitude squared a^2 .

4.4. The second-order amplitude

The magnitude of wave amplitudes is of interest, too. First of all, the exponent in Eqs. (42) and (43) indicates that both the first- and second-order amplitudes decrease in the direction of wave propagation in the presence of damping $\sigma + \zeta$.

Secondly, we take a more detailed look at the second-order amplitude by assuming zero damping for perspicuity, as Eq. (45). The second-order amplitude Eq. (43) is also positively defined: the numerator is certainly positive; the denominator is always positive although it contains a negative term. Fig. 5 shows the denominator in Eq. (43) over a large range of wave numbers. The denominator is always larger than zero. It demonstrates that a singularity is not possible mathematically and that resonance and an unbounded amplitude cannot occur, as we would expect from a physical point of view.

Fig. 6 illustrates the variation of the second-order amplitude with the wave number k and the first-order amplitude a . One can observe that the second-order amplitude monotonically increases with any single one of these two parameters. It is also noticeable that the nonlinear amplitude increases slowly with the wave number but fast with the linear amplitude.

The ratio of the second-order amplitude to the first one can be obtained through dividing the non-oscillating part of Eq. (43) by that of Eq. (42) and assuming zero damping. As expected, the perturbation, $\epsilon = (ak)^2 \ll 1$, scales the ratio's magnitude. It demonstrates that the nonlinear part of the amplitude is a small term in the order of the wave slope squared.

Fig. 7 compares the amplitude ratios the of nonlinear wave component over the linear wave component. The ratio of the present work is calculated by the amplitude of Eq. (43) divided by a_0 . The other ratio is manually measured from Fig. 6 of Ma et al. (2020). The comparison indicates that resonance does not occur in our derived solution under the assumption of infinite length that is made by both the present work and the work of Ma et al. (2020). Our analytical solution is different from theirs, although they both concern the nonlinear FSI of a floating sheet in waves. Their model focused on nonlinear water waves because steeper waves are the major risk for VLFS; our model concentrates on the structural nonlinearity considering that the water surface slope is small some distance away from the edges of the structure, because highly restricted by the LPOFPV, but large enough that structural nonlinearity cannot be neglected.

By using the parameters shown in Table 1 and fixing the wave steepness $ak = 0.1$ (rather than only the amplitude a), Fig. 8 gives a comparison of ratios of nonlinear wave amplitude over linear wave amplitude for Cases A and B over a large range of periods. The ordinate is the amplitude ratio, which is non-dimensional; the abscissa is the dimensionless wave period, which includes all the characteristic parameters for Cases A and B. Three remarks with respect to their mechanical difference can be made. First, the nonlinear waves are small, which implies that linear waves dominate the hydro-elastic wave propagation. Second, the nonlinear waves in our derived solution show a single maximum for both cases. Last, the dimensionless period at which the peak occurs in the two cases indicates that the coupled system with the plate A has a larger response to relatively long-period waves, while the coupled system with the membrane B responds to relatively short-period waves.

5. Conclusion

This article theoretically investigates the nonlinear wave propagation in the support structure of large-scale polymer offshore floating photovoltaics (LPOFPV), using a fluid–structure interaction (FSI)

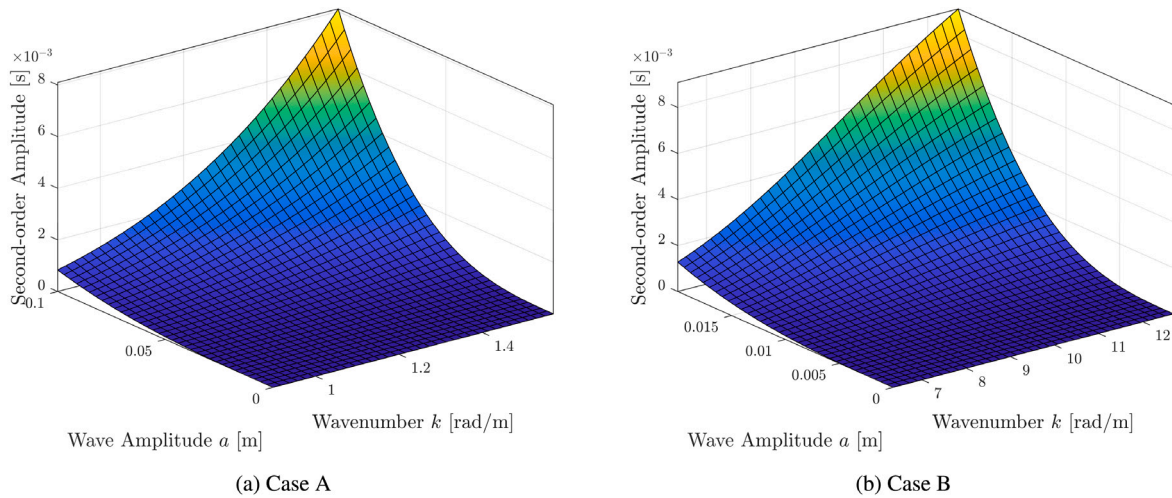


Fig. 6. The second-order amplitude calculated by Eq. (43) in Case A and Case B. The wavenumber and the first-order amplitude vary within the same range of Case A and Case B, respectively.

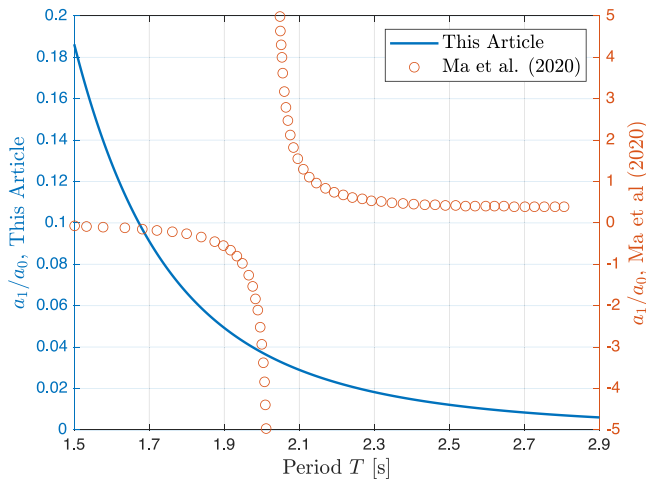


Fig. 7. Comparison of $\frac{a_1}{a_0}$, the amplitude ratios. $a_0 = 0.1$ is fixed for consistency between Eq. (43) and Ma et al. (2020).

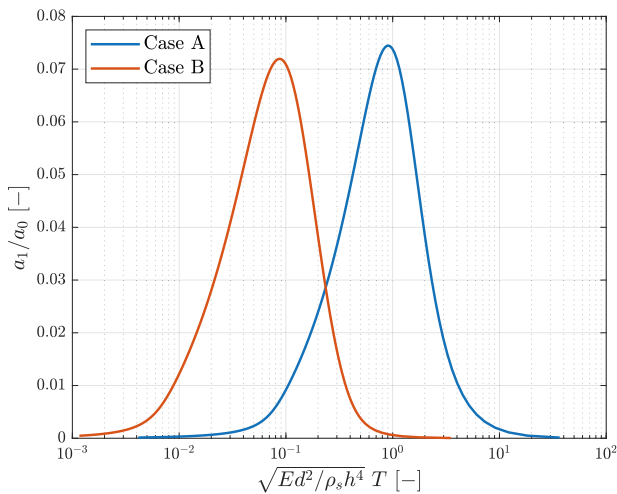


Fig. 8. Comparison of amplitude ratios of two cases in terms of dimensionless wave period.

model. The authors propose to model the considered problem by coupling a nonlinear Euler Bernoulli–von Kármán (EBVK) beam with linear Airy waves. The proposed model can be seen as complementary to the recently developed analytical model of Ma et al. (2020) that couples a linear Euler Bernoulli (EB) beam and a second-order nonlinear wave. The theoretical solution is derived with the multi-time-scale perturbation method, in which the square of the wave slope is introduced as the small perturbation. Based on the asymptotic solution, the authors present and compare results under two representative conditions, one being a pontoon-type structure representative of very large floating structures (VLFS) and the other one being a membrane-type structure representative of LPOFPV. The nonlinear solution provides expressions of the first- and second-order waves and the dispersion relation in closed forms. The following conclusions can be drawn.

- I The EBVK theory is better applicable to LPOFPV in waves than EB theory, because of the larger transverse deformation and non-negligible membrane force.
- II A fully analytic solution is derived for the proposed infinite FSI model, which is applicable to both pontoon-type and membrane-type LPOFPV.
- III The small damping does not affect the dispersion relation up to second-order but only leads to exponential attenuation of the wave amplitude in the direction of wave propagation.
- IV The derived analytical solution demonstrates that resonance does not occur in the considered FSI model in an infinite domain.

The proposed analytic approach can be extended to a fully nonlinear model coupling the EBVK beam and Stokes waves. However, a nonlinear interface condition considerably increases the complexity of the hierarchical partial differential equations and the corresponding solution. Therefore, we leave a fully nonlinear model for the future.

CRedit authorship contribution statement

Pengpeng Xu: Conceptualization, Methodology, Formal analysis, Writing – original draft, Visualization, Funding acquisition. **Peter R. Wellens:** Methodology, Formal analysis, Writing – review & editing, Supervision, Project administration.

Declaration of competing interest

The authors declare that they have no known competing financial interests or personal relationships that could have appeared to influence the work reported in this paper.

Acknowledgment

This research is financially supported by the China Scholarship Council with project NO. 201707720039.

References

- Athanassoulis, M.A., Belibassakis, K., 2009. A novel coupled-mode theory with application to hydroelastic analysis of thick, non-uniform floating bodies over general bathymetry. *Proc. Inst. Mech. Eng. M* 223 (3), 419–438. <http://dx.doi.org/10.1243/14750902JEME150>.
- Balmforth, N.J., Craster, R.V., 1999. Ocean waves and ice sheets. *J. Fluid Mech.* 395, 89–124. <http://dx.doi.org/10.1017/S0022112099005145>.
- Banks, H.T., Wang, Y., Inman, D.J., 1994. Bending and shear damping in beams: Frequency domain estimation techniques. *J. Vib. Acoust.* 116 (2), 188–197. <http://dx.doi.org/10.1115/1.2930411>.
- Belibassakis, K.A., Athanassoulis, G.A., 2005. A coupled-mode model for the hydroelastic analysis of large floating bodies over variable bathymetry regions. *J. Fluid Mech.* 531, 221–249. <http://dx.doi.org/10.1017/S0022112005004003>.
- Chen, X.J., Jensen, J.J., Cui, W.C., Fu, S.X., 2003. Hydroelasticity of a floating plate in multidirectional waves. *Ocean Eng.* 30 (15), 1997–2017. [http://dx.doi.org/10.1016/S0029-8018\(03\)00020-9](http://dx.doi.org/10.1016/S0029-8018(03)00020-9).
- Cheng, Z., Gao, Z., Moan, T., 2018. Hydrodynamic load modeling and analysis of a floating bridge in homogeneous wave conditions. *Mar. Struct.* 59, 122–141. <http://dx.doi.org/10.1016/j.marstruc.2018.01.007>.
- Cheng, Y., Ji, C., Zhai, G., Gaidai, O., 2016a. Hydroelastic analysis of oblique irregular waves with a pontoon-type VLFS edged with dual inclined perforated plates. *Mar. Struct.* 49, 31–57. <http://dx.doi.org/10.1016/j.marstruc.2016.05.008>.
- Cheng, Y., Ji, C., Zhai, G., Oleg, G., 2016b. Dual inclined perforated anti-motion plates for mitigating hydroelastic response of a VLFS under wave action. *Ocean Eng.* 121, 572–591. <http://dx.doi.org/10.1016/j.oceaneng.2016.05.044>.
- Cheng, Y., Ji, C., Zhai, G., Oleg, G., 2017. Fully nonlinear numerical investigation on hydroelastic responses of floating elastic plate over variable depth sea-bottom. *Mar. Struct.* 55, 37–61. <http://dx.doi.org/10.1016/j.marstruc.2017.04.005>.
- Cheng, Y., Zhai, G.-j., Ou, J., 2014. Time-domain numerical and experimental analysis of hydroelastic response of a very large floating structure edged with a pair of submerged horizontal plates. *Mar. Struct.* 39, 198–224. <http://dx.doi.org/10.1016/j.marstruc.2014.07.007>.
- Chia, C.Y., 1980. *Nonlinear Analysis of Plates*. McGraw-Hill International Book Company.
- Dingemans, M.W., 1997. *Water Wave Propagation over Uneven Bottoms*. vol. 13, World Scientific.
- Forbes, L.K., 1986. Surface waves of large amplitude beneath an elastic sheet. Part 1. High-order series solution. *J. Fluid Mech.* 169, 409–428. <http://dx.doi.org/10.1017/S0022112086000708>.
- Forbes, L.K., 1988. Surface waves of large amplitude beneath an elastic sheet. Part 2. Galerkin solution. *J. Fluid Mech.* 188, 491–508. <http://dx.doi.org/10.1017/S0022112088000813>.
- Iijima, K., Fujikubo, M., 2018. Hydro-elastoplastic behaviour of VLFS under extreme vertical bending moment by segmented beam approach. *Mar. Struct.* 57, 1–17. <http://dx.doi.org/10.1016/j.marstruc.2017.09.008>.
- Iijima, K., Fujikubo, M., 2019. Analytical formula for collapse extent of VLFS under extreme vertical bending moment. *J. Mar. Sci. Technol.* 24 (2), 372–381. <http://dx.doi.org/10.1007/s00773-018-0555-1>.
- Ikhennicheu, M., Danglade, B., Pascal, R., Arramounet, V., Trébaol, Q., Gorintin, F., 2021. Analytical method for loads determination on floating solar farms in three typical environments. *Sol. Energy* <http://dx.doi.org/10.1016/j.solener.2020.11.078>.
- Ilyas, M., Meylan, M.H., Lamichhane, B., Bennetts, L.G., 2018. Time-domain and modal response of ice shelves to wave forcing using the finite element method. *J. Fluids Struct.* 80, 113–131. <http://dx.doi.org/10.1016/j.jfluidstructs.2018.03.010>.
- Jain, S., Tiso, P., Haller, G., 2018. Exact nonlinear model reduction for a von Kármán beam: Slow-fast decomposition and spectral submanifolds. *J. Sound Vib.* 423, 195–211. <http://dx.doi.org/10.1016/j.jsv.2018.01.049>.
- Jang, T.S., 2013. A new semi-analytical approach to large deflections of Bernoulli-Euler-v. Karman beams on a linear elastic foundation: Nonlinear analysis of infinite beams. *Int. J. Mech. Sci.* 66, 22–32. <http://dx.doi.org/10.1016/j.ijmecsci.2012.10.005>.
- Karperaki, A.E., Belibassakis, K.A., 2021. Hydroelastic analysis of very large floating structures in variable bathymetry regions by multi-modal expansions and FEM. *J. Fluids Struct.* 102, 103236. <http://dx.doi.org/10.1016/j.jfluidstructs.2021.103236>.
- Koley, S., 2020. Water wave scattering by floating flexible porous plate over variable bathymetry regions. *Ocean Eng.* 214, 107686. <http://dx.doi.org/10.1016/j.oceaneng.2020.107686>.
- Krysko, V.A., Awrejcewicz, J., Papkova, I.V., Saltykova, O.A., Krysko, A.V., 2018. On reliability of chaotic dynamics of two Euler-Bernoulli beams with a small clearance. *Int. J. Non-Linear Mech.* 104, 8–18. <http://dx.doi.org/10.1016/j.ijnonlinmec.2017.11.013>.
- Liu, X., Wang, X., Xu, S., 2020. A DMM-EMM-RSM hybrid technique on two-dimensional frequency-domain hydroelasticity of floating structures over variable bathymetry. *Ocean Eng.* 201, 107135. <http://dx.doi.org/10.1016/j.oceaneng.2020.107135>.
- Ma, C., Iijima, K., Oka, M., 2020. Nonlinear waves in a floating thin elastic plate, predicted by a coupled SPH and FEM simulation and by an analytical solution. *Ocean Eng.* 204, 107243. <http://dx.doi.org/10.1016/j.oceaneng.2020.107243>.
- Magkouris, A., Belibassakis, K., Rusu, E., 2021. Hydrodynamic analysis of twin-hull structures supporting floating PV systems in offshore and coastal regions. *Energies* 14 (18), <http://dx.doi.org/10.3390/en14185979>.
- Meylan, M.H., 2021. Time-dependent motion of a floating circular elastic plate. *Fluids* 6 (1), 29. <http://dx.doi.org/10.3390/fluids6010029>.
- Ocean Sun, 2021. Ocean Sun projects. <https://oceansun.no/projects/>. (Accessed 18 March 2021).
- Paavani, D., Aswathy, M., Arun, C.O., Krishna, I.R.P., 2020. Analysis of geometrically nonlinear Euler-Bernoulli beam using EFGM. *IOP Conf. Ser.* 936, 012050. <http://dx.doi.org/10.1088/1757-899x/936/1/012050>.
- Papathanasiou, T.K., Belibassakis, K.A., 2014. Hydroelastic analysis of VLFS based on a consistent coupled-mode system and FEM. *IES J. A* 7 (3), 195–206. <http://dx.doi.org/10.1080/19373260.2014.922037>.
- Părău, E., Dias, F., 2002. Nonlinear effects in the response of a floating ice plate to a moving load. *J. Fluid Mech.* 460, 281–305. <http://dx.doi.org/10.1017/S0022112002008236>.
- Ren, N., Zhang, C., Magee, A.R., Hellan, Ø., Dai, J., Ang, K.K., 2019. Hydrodynamic analysis of a modular multi-purpose floating structure system with different outermost connector types. *Ocean Eng.* 176, 158–168. <http://dx.doi.org/10.1016/j.oceaneng.2019.02.052>.
- Riyansyah, M., Wang, C.M., Choo, Y.S., 2010. Connection design for two-floating beam system for minimum hydroelastic response. *Mar. Struct.* 23 (1), 67–87. <http://dx.doi.org/10.1016/j.marstruc.2010.01.001>.
- Sahu, A., Yadav, N., Sudhakar, K., 2016. Floating photovoltaic power plant: A review. *Renew. Sustain. Energy Rev.* 66, 815–824. <http://dx.doi.org/10.1016/j.rser.2016.08.051>.
- Schreier, S., Jacobi, G., 2020. Experimental investigation of wave interaction with a thin floating sheet. In: *Proceedings of the International Offshore and Polar Engineering Conference*, vol. 2020-October, pp. 2479–2488.
- Schwartz, L.W., 1974. Computer extension and analytic continuation of Stokes' expansion for gravity waves. *J. Fluid Mech.* 62 (3), 553–578. <http://dx.doi.org/10.1017/S0022112074000802>.
- Singla, S., Martha, S.C., Sahoo, T., 2018. Mitigation of structural responses of a very large floating structure in the presence of vertical porous barrier. *Ocean Eng.* 165, 505–527. <http://dx.doi.org/10.1016/j.oceaneng.2018.07.045>.
- Suzuki, H., Riggs, H.R., Fujikubo, M., Shugar, T.A., Seto, H., Yasuzawa, Y., Bhattacharya, B., Hudson, D.A., Shin, H., 2006. Very large floating structures. In: *ASME 2007 26th International Conference on Offshore Mechanics and Arctic Engineering*. In: *Structures, Safety and Reliability; Petroleum Technology Symposium*, vol. 2, pp. 597–608. <http://dx.doi.org/10.1115/omae2007-29758>.
- Suzuki, H., Yoshida, K., Iijima, K., 1996. A consideration of the structural design of a large-scale floating structure. *J. Mar. Sci. Technol.* 1 (5), 255–267. <http://dx.doi.org/10.1007/BF02390724>.
- Trapani, K., Redón Santafé, M., 2015. A review of floating photovoltaic installations: 2007–2013. *Prog. Photovolt., Res. Appl.* 23 (4), 524–532. <http://dx.doi.org/10.1002/pip.2466>.
- Vadlamani, S., Arun, C.O., 2019. Construction of beam elements considering von Kármán nonlinear strains using B-spline wavelet on the interval. *Appl. Math. Model.* 68, 675–695. <http://dx.doi.org/10.1016/j.apm.2018.11.042>.
- Vanden-Broeck, J.-M., Părău, E.I., 2011. Two-dimensional generalized solitary waves and periodic waves under an ice sheet. *Phil. Trans. R. Soc. A* 369 (1947), 2957–2972. <http://dx.doi.org/10.1098/rsta.2011.0108>.
- Wang, C.D., Meylan, M.H., 2002. The linear wave response of a floating thin plate on water of variable depth. *Appl. Ocean Res.* 24 (3), 163–174. [http://dx.doi.org/10.1016/S0141-1187\(02\)00025-1](http://dx.doi.org/10.1016/S0141-1187(02)00025-1).
- Xu, P., Wellens, P., 2021. Effects of static loads on the nonlinear vibration of circular plates. *J. Sound Vib.* 504, 116111. <http://dx.doi.org/10.1016/j.jsv.2021.116111>.
- Yesudian, A.N., Dawson, R.J., 2021. Global analysis of sea level rise risk to airports. *Clim. Risk Manag.* 31, 100266. <http://dx.doi.org/10.1016/j.crm.2020.100266>.
- Zhang, H.C., Xu, D.L., Lu, C., Qi, E.R., Tian, C., Wu, Y.S., 2017. Connection effect on amplitude death stability of multi-module floating airport. *Ocean Eng.* 129, 46–56. <http://dx.doi.org/10.1016/j.oceaneng.2016.11.011>.